THE JOURNAL OF PHYSICAL CHEMISTRY C

Article

pubs.acs.org/JPCC

Silver-Overgrowth-Induced Changes in Intrinsic Optical Properties of Gold Nanorods: From Noninvasive Monitoring of Growth Kinetics to Tailoring Internal Mirror Charges

Moritz Tebbe,[†] Christian Kuttner,[†] Martin Mayer,[†] Max Maennel,[†] Nicolas Pazos-Perez,[†,‡] Tobias A.F. König,*[,†] and Andreas Fery*[,†]

[†]Physical Chemistry II, University of Bayreuth, Universitätsstraße 30, 95447 Bayreuth, Germany

[‡]Departamento de Quimica Fisica e Inorganica, Universitat Rovira i Virgili and Centro de Tecnologia Quimica de Cataluña, Carrer de Marcel·lí Domingo s/n, 43007 Tarragona, Spain

Supporting Information

ABSTRACT: We investigate the effect of surfactant-mediated, asymmetric silver overgrowth of gold nanorods on their intrinsic optical properties. From concentration-dependent experiments, we established a close correlation of the extinction in the UV/vis/NIR frequency range and the morphological transition from gold nanorods to Au@Ag cuboids. Based on this correlation, a generic methodology for *in situ* monitoring of the evolution of the cuboid morphology was developed and applied in time-dependent experiments. We find that growth rates are sensitive to the substitution of the surfactant headgroup by comparison of benzylhexadecyldimethylammonium chloride (BDAC) with hexadecyltrimethylammonium chloride (CTAC). The time-dependent overgrowth in BDAC proceeds about 1 order of magnitude slower than in CTAC, which allows for higher control during silver overgrowth. Furthermore, silver overgrowth results in a qualitatively novel optical feature: Upon excitation inside the overlap region of the interband transition of gold and intraband of silver, the gold core acts as a retarding element. The much higher damping of the gold core compared to the silver shell in Au@Ag cuboids induces mirror charges at the core/shell interface as shown by electromagnetic simulations. Full control over the kinetic growth process consequently allows for precise tailoring of the resonance wavelengths of both modes. Tailored and asymmetric silver-overgrown gold nanorods are of particular interest for large-scale fabrication of nanoparticles with intrinsic metamaterial properties. These building blocks could furthermore find application in optical sensor technology, light harvesting, and information technology.

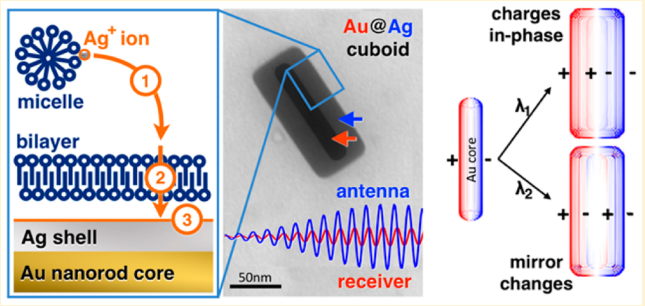

INTRODUCTION

Control over metallic nanoparticle morphology and composition gained increasing significance with respect to tailoring localized surface plasmon resonances (LSPRs). That makes noble metal nanoparticles excellent candidates for potential application as building blocks for metamaterial applications,[1,2] in optical sensing,[3,4] information technology,[5,6] and energy harvesting.[7,8] In optical metamaterials, a negative index of refraction can be produced combining a negative electric permittivity with a negative magnetic permeability at the same wavelength for building blocks (meta-atoms) much smaller than the used wavelength.[9] Major efforts have been spent in designing resonator structures (e.g., split ring resonators), which consist of an inductor−capacitor loop, a fundamental building block for fabrication of metamaterials with negative index of refraction.[10,11] These structures are restricted by small scale and expensive top-down methods such as electron beam lithography or focused ion beam milling.[12] To make widespread applications feasible, bottom-up methods are necessary, such as template-assisted self-assembly.[13,14] For bottom-up assembly a redesign of the applied plasmonic nanoparticle is crucial.[15] Stacked nanoparticle pairs or substrate-supported mirror charges are promising approaches for meta-atoms with so-called extrinsic metamaterial properties, only present when assembled in distinct geometrical configurations.[16,17]

An alternative approach is the assembly of preformed meta-atoms with intrinsic metamaterial properties.[18] Such meta-atoms can be achieved by amorphous metal overgrowth of dielectric core particles[19,20] or by tailored synthesis of metal−core/metal−shell particles[21−24] with a clear signature of mirror charges at the core/shell interface. These mirror charges can be excited with an antenna particle into a receiver particle as it has been shown for pairs of nanoparticles[17] or metallic film-coupled nanoparticles.[16] Core/shell particles could be realized by high-precision asymmetric overgrowth and subsequent facet-selective etching.[25−27] Mirror charges at

Received: April 1, 2015
Revised: April 11, 2015
Published: April 12, 2015

DOI: 10.1021/acs.jpcc.5b03155
J. Phys. Chem. C 2015, 119, 9513−9523

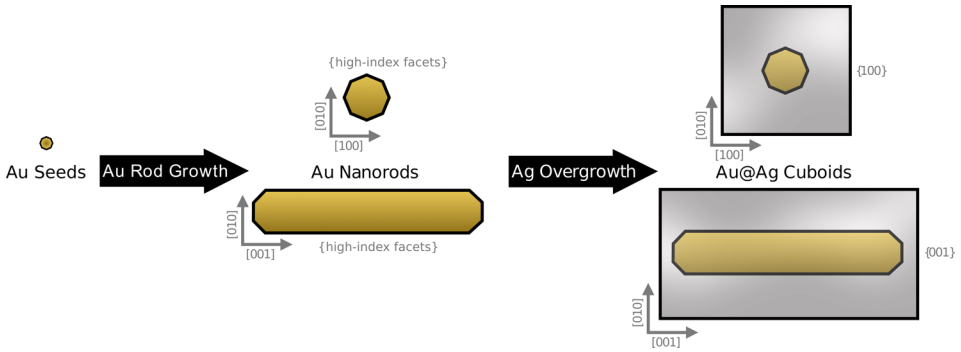

Figure 1. Schematic depiction of the synthetic pathway to Au@Ag cuboids: CTAB-stabilized spherical single-crystalline seed nanoparticles are grown into rods using CTAB and $AgNO_3$ as directing agents and HQ as reducing agent. In a second, step the as-prepared gold nanorods are transferred to desired surfactants (BDAC, CTAC) and subsequently overgrown with silver into Au@Ag cuboids.[22,48,49,75]

metal−/metal interfaces are induced by excitation inside the overlap region of the interband of gold (core) and intraband of silver (shell) between 326 and 515 nm wavelengths. Below its interband transition, gold acts as a retarding element because of the much higher damping compared to silver at the same wavelength. This asymmetry facilitates induction of mirror charges at the core/shell interface, which transforms gold−core/silver−shell nanoparticles (Au@Ag cuboids) into potential meta-atoms.

Well-defined gold/silver core/shell particles with a cuboidal morphology can be synthesized in large quantities in a three-step process based on surfactant-mediated seeded-growth approach.[28,29] First single-crystalline seed nanoparticles are formed and in a second step grown into single-crystalline gold nanorods.[30] These nanorods are subsequently overgrown with silver to form Au@Ag cuboids.[22] In general, fine-tuning of nanoparticle morphology requires to adjust parameters like seed crystallinity,[31,32] metal ion feed,[33] type and amount of reducing agent and surfactants, and application of ancillary additives.[30,34−37] Especially, the choice of the counterion of the surfactant is crucial owing to preferential adsorption to specific crystallographic facets.[24,38−40] Differences in adsorption affinity are attributed to changes in surface energy which can be utilized to direct nanoparticle growth.[24,41,42] Gold−core/silver−shell nanoparticles in various morphologies can be prepared with high spatial precision from gold seeds exhibiting well-defined crystallinity by epitaxial overgrowth with silver.[22,23,25,26,43−48] In the presence of chloride ions, silver overgrowth takes place preferentially at crystal planes of higher index facets such as {110}, {111}, and {520}.[22] Single-crystalline gold nanorods with an octagonal cross section are initially covered by eight lateral high-index facets.[49] Such nanocrystals grow into Au@Ag cuboids enclosed by six well-defined thermodynamically stable low-index {100} facets (see Figure 1).[22,25,48] After the transition from octagonal to rectangular cross section, the system tends to reduce the free surface energy.[27] Thus, silver deposition preferentially takes place on its lateral facets.[22,48]

Consequently, it is evident that the choice of surfactant, apart from stabilizing the nanoparticles, is crucial for particle shape and monodispersity.[28,36,37,50] Three main contributions have been assigned to the surfactant: growth direction, complex formation with metal ions, and bilayer formation at the nanocrystal surface.[32,51−54] Aromatic compounds can be exploited in order to reduce the amount of impurities and reduce size dispersity in gold nanorod synthesis.[28,30,31,34,35,55] Benzyl-substituted surfactants like benzylhexadecyldimethylammonium chloride (BDAC) or aromatic additives like 5-bromosalicylic acid strongly influence nanoparticle synthesis.[28,34,35] Derivatives of phenole, e.g. hydroquinone, can act as weak reducing agents and thus are able to reduce metal ions.[30,34,35] Furthermore, aromatic compounds have been reported to influence the bilayer formation owing to hydrophobic and attractive $\pi-\pi$ interactions.[56,57] As a consequence, aromatic surfactants may affect the micellar aggregation number and the critical micelle concentration and alter the packing density of the bilayer.[50,58,59] Even though there are several studies on growth kinetics of anisotropic nanoparticles reported in the literature,[35,36,54,60−67] little is reported on the specific influence of aromatic moieties at cationic surfactant headgroups.[47] The challenge is the fundamental understanding how aromatics influence the reaction kinetics and if their influence is more related to complex formation, bilayer formation, diffusion, or all three combined.

So far, studies on the kinetics of the growth processes were mainly performed on solid substrates by tracking the growth of individual nanoparticles with sophisticated spectroscopic methods.[64−66,68] Methods like small-angle X-ray scattering (SAXS) and conventional UV/vis/NIR extinction spectroscopy were utilized to gain information about the kinetics of particle ensembles.[35,36,42,47,60−63,67,69−71] Especially, UV/vis/NIR spectroscopy is accessible to a broad scientific community and allows for noninvasive growth monitoring with a high temporal resolution. Deriving morphological features for complex objects like overgrown nanoparticles, however, requires a solid understanding of the correlation of the spectroscopic response and the morphological changes during growth. A better understanding of the overgrowth kinetics will allow for increased control within nanoparticle synthesis and lead to a more rational molecular design of suitable surfactants.

In this work, we present the surfactant-controlled overgrowth of gold nanorods into gold−core/silver−shell nanoparticles (Au@Ag cuboids) to gain low growth rates for full control of the kinetic process. We chose two surfactants with the same counterion, but with different headgroup substituents, i.e., benzylhexadecyldimethylammonium chloride (BDAC) and hexadecyltrimethylammonium chloride (CTAC), to synthesize Au@Ag cuboids. While BDAC offers lower growth rates, which is favorable for nanoparticle synthesis, CTAC serves as a reference system to further enhance our understanding of the silver-shell growth kinetics. We link the results from electromagnetic simulation precisely with the UV/vis/NIR extinction to provide information about morphology at each step of the

DOI: 10.1021/acs.jpcc.5b03155
J. Phys. Chem. C 2015, 119, 9513−9523

overgrowth process and uncover transient morphological changes. Furthermore, we evaluate the formation of intrinsic mirror charge signatures at the core/shell interface for potential application in metamaterials.

EXPERIMENTAL SECTION

Materials. All chemicals were purchased from Sigma-Aldrich unless mentioned otherwise: sodium borohydride ($NaBH_4$, ≥99.99%), gold(III) chloride trihydrate ($HAuCl_4 \cdot 3H_2O$, ≥99.9%), silver(I) nitrate ($AgNO_3$, ≥99.9%), hexadecyltrimethylammonium bromide (CTAB, 99%, Merck), hexadecyltrimethylammonium chloride (CTAC, Molekula), benzyldimethylhexadecylammonium chloride (BDAC, Molekula), ascorbic acid (AA, ≥99.0%), and hydroquinone (HQ, ≥99%) were used as received without further purification. All solutions were freshly prepared except for gold stock solution and used without further purification. Water was purified using a Milli-Q system (Millipore). The final resistivity was 18.2 MΩ·cm.

Characterization. UV/vis/NIR spectra were recorded at a Jasco V-670 (US-MD) with a temperature control unit. Nanoparticle solutions were dissolved 10 times with the respective surfactant to reduce extinction. TEM images were obtained with a LEO CEM902 operating at an acceleration voltage of 80 kV and with a LEO 922 OMEGA EFTEM with an acceleration voltage of 200 kV from Zeiss (Germany). Zero-loss filtered images were recorded using a bottom mounted Ultrascan 1000 (Gatan) CCD camera system. Gatan Digital Micrograph 3.9 for GMS 1.4 software was used for image acquisition. For TEM analysis 1 mL of nanoparticle solutions were concentrated to 100 μL via centrifugation and washed twice to adjust the surfactant concentration to 1 mM. 5 μL of the as-prepared solution was dried on Quantifoil 300 mesh copper grid with carbon films. Measurements performed for edge sharpening evaluation (Figure 4) were prepared under a N_2 environment. For size evaluation the software ImageJ (version 1.44p, U.S. National Institutes of Health) was used.

Seed Synthesis. Seeds were prepared as reported elsewhere with small variations.[30] Briefly, 5 mL of an aqueous 0.5 mM $HAuCl_4$ solution was added to 5 mL of an aqueous 0.2 M CTAB solution and stirred for 10 min. The solution was vigorously stirred at 1200 rpm, and 600 μL of a freshly prepared 0.01 M $NaBH_4$ solution was added quickly. The solution was stirred for 2 min and aged for another 30 min.

HQ-Based Synthesis of Gold Nanorods. Nanorods with an AR of 5.5 were prepared following a procedure published recently by Vigdermann and Zubarev.[30] Briefly, to 250 mL of an aqueous 0.1 M CTAB solution 1250 μL of a 0.1 M $HAuCl_4$ stock solution was added to yield a final concentration of 0.5 mM. Afterward, 1250 μL of an aqueous 0.1 M $AgNO_3$ solution was added, followed by the addition of 12.5 mL of an aqueous 0.1 M HQ solution. The solution was stirred at 600 rpm at 32 °C, yielding a colorless solution. To induce nanorod growth, 6 mL of the as-prepared seed solution was added followed by vigorous shaking. The solution was stored at 32 °C overnight.

Silver Overgrowth. Overgrowth was performed according to a protocol published recently by Gomez-Graña et al. and others.[22,45,46,72] Briefly, as-prepared seeds were centrifuged at 8500 rcf for 30 min and transferred to a 10 mM surfactant solution. Subsequently, they were washed six times with a 10 mM surfactant solution to ensure full surfactant exchange. To 5 mL of 0.25 mM nanorod seeds in 10 mM surfactant solution varied amounts (2.5−100 μL) of a 0.1 M $AgNO_3$ solution were added to adjust the final Ag concentration to a desired value (0.05−2 mM) (see also Table S2). The solution was heated to 60 °C and stirred at a constant rate of 600 rpm. To initiate the reduction, an aqueous 0.4 M AA solution was added. The amounts were the same as for $AgNO_3$ to ensure a 4 times molar AA excess. The reactions were allowed to proceed at 60 °C for 8 h.

Kinetic Experiments. Dynamic overgrowth experiments were performed similar to static overgrowth experiments. Briefly, as-prepared seed nanorods were transferred to a 10 mM surfactant solution by centrifugation at 8500 rcf for 30 min and washed six times with a 10 mM surfactant solution to ensure full surfactant exchange. To 5 mL of seed solution containing 0.25 mM gold 100 μL of a 0.1 M $AgNO_3$ solution was added to adjust the final silver concentration to 2 mM. The solutions were heated to 60 °C and stirred at a constant rate of 600 rpm. To initiate the reduction, 100 μL of a 0.4 M AA solution was added. The reactions performed within UV/vis/NIR cuvettes were diluted 5 times with the specific 10 mM surfactant solution and were allowed to proceed at 60 °C for 14 h.

FDTD Simulations. Extinction spectra were simulated using a commercial software from Lumerical Solutions, Inc. (FDTD Solutions, Version 8.7.3). First, we modeled the gold nanorods (82 nm times 15 nm) in water (n = 1.333) with different amounts of cap rounding (Figure S2), which is defined by an ellipsoid with fixed first radius (nanorod width) and a variable second radius. In agreement with experimental peak positions, we chose a cap radius of 5 nm. The nanorods dimensions were evaluated using TEM images (Figure S1). For a broadband source simulation (total-field scattered-field source, λ = 300−1300 nm), the FDTD software approximates the refractive index of the materials by a polynomial function. For the optical constants of Au, a fitting of the experimental data by Johnson and Christy (JC) was applied (six coefficients, one imaginary weight: 0.211 RMS error).[73] Second, the pure Ag cuboid was modeled with an edge radius of 8% of the cuboid length. Third, the Au@Ag cuboid was modeled with dimensions (82−92 nm × 15−38 nm) as evaluated from TEM images (Figure S3). For the Ag permittivity, material data from Hagemann et al. (CRC) were used (five coefficients, two imaginary weight: 0.187 RMS error).[74] The parameters for the simulation performed for the kinetic plot are summarized in Table S1. A mesh size of 0.5 nm was chosen, and the zero-conformal-variant mesh refinement was used. For the best simulation stability, the mesh area was chosen to be 50 nm larger than the existing structure in all three principal directions. All simulations reached the auto shut-off level of 10^{-5} before reaching 150 fs simulation time. Antisymmetric boundary conditions (BC) were used normal to the polarization plane, and symmetric BC were used parallel to the polarization plane. In radiation direction we used in both directions the perfect match layer BC. To determine the surface charge densities, we simulated the model at the plasmonic mode frequency at a pulse length of ∼20 fs (optimized for long pulse length).

RESULTS AND DISCUSSION

Synthesis and Optical Properties of Au@Ag Cuboids. Au@Ag cuboids are prepared in two steps. Single-crystalline gold nanorods were synthesized followed by a subsequent overgrowth with silver (see Figure 1). The gold nanorod cores used for surfactant-controlled silver overgrowth were prepared following a protocol published recently by Vigderman and Zubarev.[30] This seed-mediated synthesis utilizes the surfactant CTAB and silver nitrate ($AgNO_3$) as growth directing agents,

DOI: 10.1021/acs.jpcc.5b03155
J. Phys. Chem. C 2015, 119, 9513−9523

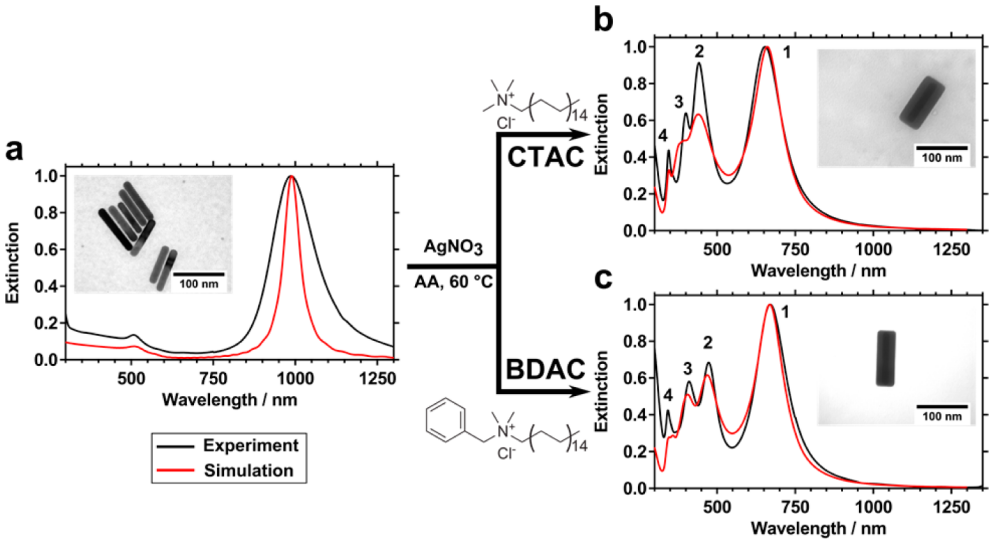

Figure 2. Normalized UV/vis/NIR extinction of (a) gold nanorod cores and Au@Ag cuboids prepared with (b) CTAC or (c) BDAC as surfactant. Simulated extinction spectra are included in red color. Insets show TEM images of the final nanoparticle morphology.

similar to the preparation of single-crystalline gold nanorods (see Figure 1).[28,29] In contrast to most widely used methods, ascorbic acid (AA) is replaced by an excess of hydroquinone (HQ).[30,55] This strongly influences the growth kinetics, since HQ is a weaker reducing agent and might also act similar to aromatic additives.[34,35] Thus, applying HQ results in high gold ion conversions (up to 100%) and low amounts of impurities making further cleaning steps obsolete.[30] The concentration of $AgNO_3$ was optimized in order to yield high aspect ratios up to 5.5. So far, aspect ratios in this range have only been reported for synthesis routes using binary mixtures of surfactants.[28,30]

As-prepared gold nanorods were used to exchange CTAB against the respective surfactant (CTAC or BDAC) for subsequent anisotropic, controlled silver overgrowth (see Figure 1). Multiple centrifugation steps were performed to ensure complete replacement of counterions (bromide against chloride). The surfactants used in this work differ in the substitution of the ammonium headgroup with BDAC containing an aromatic benzyl group instead of a methyl group for CTAC (see Figure 2). Recently, Zhang and co-workers reported on the morphology of gold nanorods prepared with HQ and phenols to be single-crystalline.[55] This finding is consistent with our results as the gold nanorods prepared with HQ grow in highly anisotropic fashion. Consequently, the single-crystalline gold nanorods possess lateral high index facets and thus grow into well-defined Au@Ag cuboids with six {100} facets (see Figure 1). The final cuboidal morphology is expected for chloride as counterion stabilizing selectively the {100} facets due to a significantly reduced surface energy of these facets compared to others as a result of an increased packing density of ions.[22] Indeed, this manner is observed for both surfactants, giving evidence that the final crystalline structure and shape of the prepared cuboids and consequently the underlying growth process are strongly constrained to the counterion.[22,25,45] At acidic conditions the intermediate ascorbate anion is the dominant species present in solution and responsible for reducing silver ions.[76,77] Consequently, the reduction rate is significantly reduced compared to basic conditions. Thus, overgrowth was performed at elevated temperature of 60 °C to increase the reducing power of AA and ensure a consistent reduction of silver ions.[22,26,72]

The gold nanorods were characterized by UV/vis/NIR spectroscopy and transmission electron microscopy (TEM) as presented in Figure 2. The nanorods display a near-infrared longitudinal mode of 988 nm and a transversal mode of 510 nm (see Figure 2a). Nanorod dimensions were determined from TEM measurements to be 82 ± 8 nm in length and 15 ± 1 nm in diameter (see Figure S1). The overall amount of impurities was below 1%, as suggested by the high intensity ratio of the longitudinal to transversal mode of 7.5.[30,36] Based on these results, finite-difference time-domain (FDTD) modeling was performed.[78] By varying the rod dimensions and tip curvature, the best agreement with the experimental data was found for a gold nanorod of 82 nm in length, 15 nm in width, and a tip radius of 5 nm (compare Figure S2). In modeling, a nanorod is constituted from a cylinder with two semiellipsoids as tips. The ellipsoid radius at the cylinder border is defined by the rod diameter while the radius in the geometric axis of the cylinder is defined as tip radius.

The UV/vis/NIR extinction spectra depicted in Figure 2b,c show syntheses performed with a molar Ag to Au ratio of 8 and either CTAC or BDAC as surfactant. The resulting spectra contain four resonance modes characteristic for cuboid or cubelike silver and gold−core/silver−shell nanoparticles.[25,44−46,72] The energetically lowest resonance mode is referred to the longitudinal mode (~610 nm), excited along the geometric axis. The energetically lowest resonance mode for a square cross section is attributed to the transversal mode (~530 nm), excited perpendicular to the geometric axis of the cuboid. The energetically highest resonance mode is just above the interband transition of silver (300 nm). Between the energetically highest and lowest plasmonic transverse mode two additional transversal modes are located (between 326 and 490 nm), which are characterized by a dominant dipolar mode and higher dipolar modes as a left shoulder. Generally, with increasing size of the particle the plasmonic modes shift toward lower energy because they are easier to polarize.[67,68] Overgrowth of gold nanorods with a silver shell results in a significant narrowing of the longitudinal plasmonic mode due to lower amount of damping and better polarizability compared

DOI: 10.1021/acs.jpcc.5b03155
J. Phys. Chem. C 2015, 119, 9513−9523

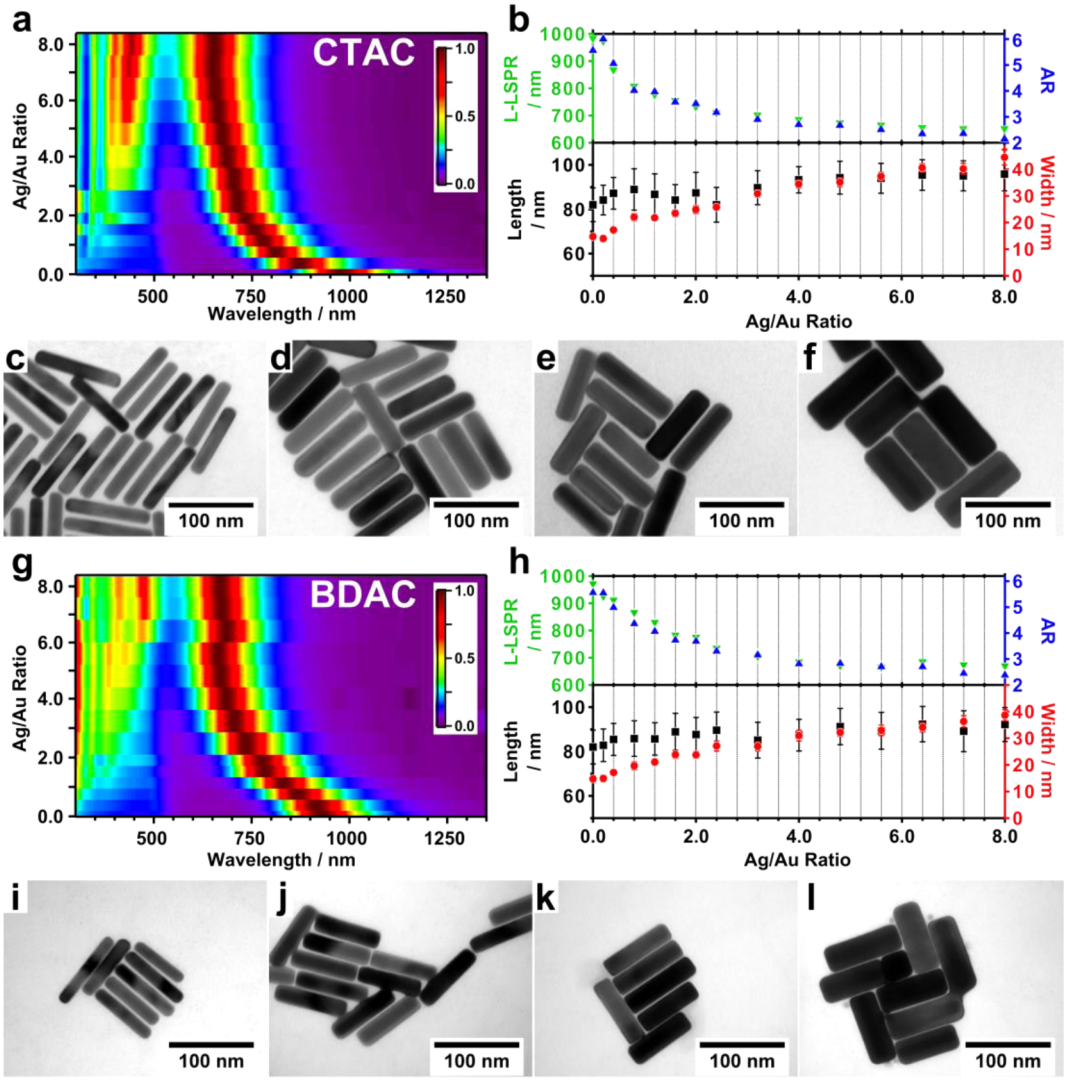

Figure 3. Au@Ag cuboid growth in static experiments: heat maps of the concentration-dependent evolution of plasmonic modes complied from normalized UV/vis/NIR extinction spectra in (a) CTAC and (g) BDAC. Longitudinal modes (L-LSPR), length, width, and corresponding aspect ratio of Au@Ag cuboids synthesized in (b) CTAC and (h) BDAC plotted versus Ag to Au ratio. TEM micrographs of Au@Ag cuboids prepared with Ag to Au ratios of 0.2, 1.2, 2, and 6.4 for (c–f) CTAC and (i–l) BDAC.

to gold. This effect is not related to changes in size distribution of nanoparticles and is referred to "plasmonic focusing".[65]

The length and width of as-prepared Au@Ag cuboids were determined to be 95 ± 8 and 45 ± 3 nm for preparation with CTAC and 92 ± 8 and 39 ± 2 nm for BDAC (see Figure S3), drastically altering the aspect ratio from 5.5 (gold nanorod cores) to around 2.1 and 2.4 for Au@Ag cuboids, respectively. The TEM images in Figure 2b,c clearly reveal that the epitaxial growth of the silver shell on gold nanorod seeds takes place almost exclusively at the lateral facets. Thus, the nanoparticles become thicker and ultimately grow into Au@Ag cuboids.[22,27,44,45,72] For the simulations presented in Figure 2b,c the best results were found for 0% and 2% edge rounding for BDAC and CTAC, respectively. We define the edge-rounding factor for a cuboid as the edge or corner radius, respectively, scaled by the length. As reported in the literature, the typical edge-rounding factor of cuboidal particles in an aqueous solution is between 8% and 16%.[79−81] The very low amount of edge rounding results in a large number of resonances and the significant red-shift of plasmonic modes (dipolar modes) compared to rounded nanostructures. Generally, the number of resonances increases as the symmetry of a structure decreases (see Figure S4).[80] We found the best agreement between the simulated spectra and the experimental measured spectra when we assume sharp edges. Consequently, the edge rounding is a good indicator for the quality of Au@Ag cuboid syntheses.

Noninvasive Monitoring of Silver Overgrowth. *In situ* monitoring by UV/vis/NIR spectroscopy allows for quantification of transient morphological changes (length, width, aspect ratio, edge rounding) *during* silver overgrowth, if quantitatively compared with detailed simulations. Therefore, we first performed static experiments (completed overgrowth at given Ag to Au ratios) to clearly correlate the morphology of Au@Ag cuboids with FDTD simulations. Second, we applied *in situ* monitoring in dynamic experiments for two surfactants with the same counterion, but with different headgroup substituents, i.e., BDAC and CTAC. Third, we established a kinetic model to describe the overgrowth mechanism.

DOI: 10.1021/acs.jpcc.5b03155
J. Phys. Chem. C 2015, 119, 9513−9523

Figure 3 shows static experiments at different Ag to Au ratios (0 to 8). This ratio ultimately limits the amount of silver deposition leading to distinct thickness of the silver shell. The dimensions of resulting cuboids were evaluated with TEM (see Figure 3 and Figure S5). Figure 3a–g presents the spectral signatures for BDAC and CTAC in dependence on the Ag to Au ratio. The remarkable similarity of the observed plasmonic responses indicates that both surfactants yield Au@Ag cuboids of identical morphology. In particular, the blue-shift of the plasmonic mode (1) from 975 to 650 nm can be precisely tailored by variation of the Ag to Au ratio. The appearance of sharp transversal modes (e.g., at ~450 nm (2)) indicates cuboids.

Figure 3b–e summarizes the morphological parameters (length, width, and aspect ratio) resulting from the choice of surfactant and Ag to Au ratio. The cuboids experience a change in aspect ratio from 6 down to 2 as they extend almost exclusively in width. The growth in length of about 10 nm is considerably below the lateral growth of up to 30 nm. Consequently, tailored overgrowth with defined Ag to Au ratio results in the identical Au@Ag cuboid morphologies, independent of the used surfactant. This intermediate result is crucial to link the spectral signature to morphological changes.

To study the influence of the surfactant on the kinetics of the overgrowth process, we conducted dynamic, *in situ* experiments at a fixed Ag to Au ratio of 8 at a temporal resolution of 5 min. Figure 4a,b shows the time-dependent UV/vis/NIR data using either CTAC or BDAC (see also Figure S6). Qualitatively, it is obvious that the conversion with CTAC proceeds much faster than with BDAC but converges into almost identical mode structures i.e., mode shifts and intensity distributions of all four modes. Therefore, we can conclude that both surfactants yield Au@Ag cuboids comparable in structure, size, and edge rounding (see Figure S7).

The dynamic experiments revealed new transient spectral features, as we will discuss in the following. Figure 4a,b shows the longitudinal dipolar plasmonic mode (1), which experiences an initial shift toward blue up to a maximum value of about 652 nm for CTAC and 663 nm for BDAC. This blue-shift is followed by a significant red-shift of mode (1) of 15 nm for CTAC and 10 nm for BDAC. At the same time the transversal modes (2), (3), and (4) arise. Upon further overgrowth, these modes increase in intensity and shift toward red.

Comparing FDTD simulation with above-mentioned results, the growth process can be divided in separated processes (see Figure 4c). The initial blue-shift of mode (1) can be attributed to the constant increase of the silver shell thickness, the corresponding change in aspect ratio, and the morphological transition from octagonal to square cross section. The subsequent significant red-shift cannot be explained by further overgrowth. We included an extended linear overgrowth (total length 101 nm and total width 55 nm) in the Supporting Information (Figure S8a). Theoretical modeling with an excellent match with the experimental observation assign this red-shift to a small change in the edge rounding, which is between 0% and 8% (Figure 4c and Figure S8b). Taking this feature (so-called edge sharpening) into account, we can describe the overgrowth process in more detail: First, the Au@Ag cuboid extends stepwise both in length and in width, from its initial seed geometry (82 nm × 15 nm) up to 92 nm × 38 nm, keeping a constant edge rounding of 8%. After that, the edge rounding is decreased in order to emulate the red-shift. Finally, an ideal structure of an Au@Ag cuboid with sharp

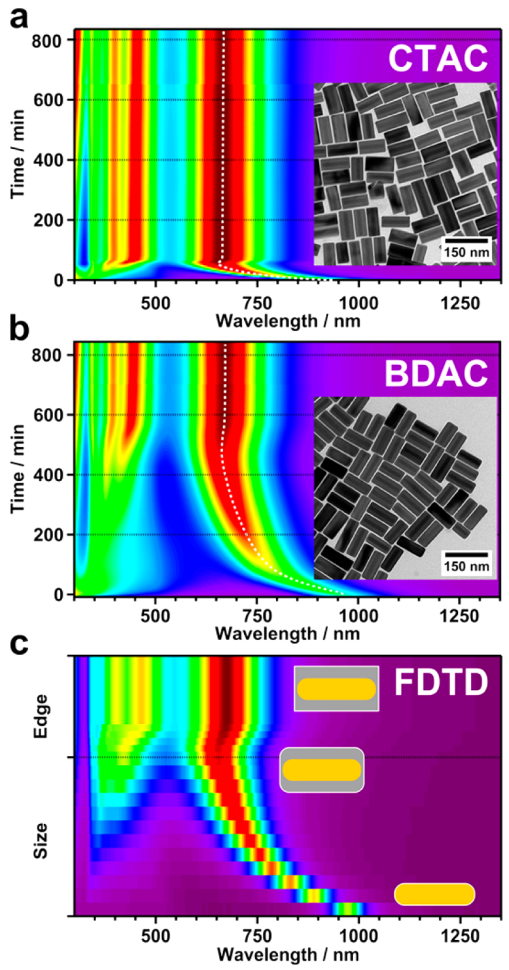

Figure 4. Au@Ag cuboid growth in dynamic experiments and compared to simulation: heat maps of time-dependent UV/vis/NIR extinction spectra of syntheses performed with (a) CTAC and (b) BDAC at Ag to Au ratio of 8 (also compare Figure S6). Representative TEM insets show the final Au@Ag cuboids. The plasmonic mode (1) features an initial blue-shift followed by a slight red-shift as highlighted by the white dashed line. (c) Modeled evolution of the spectral signature considering both changes in dimension (size) and edge rounding (edge) (for simulation parameters see Table S1).

edges and final dimensions of 92 nm × 38 nm is formed and maintained. These results were evidenced by additional TEM measurements performed under inert gas conditions during sample preparation to suppress rapid oxidation/sulfidation of silver in air as observed for static experiments (see Figure 3). TEM micrographs shown in Figure 4 as insets reveal sharp edges obtained for both surfactants, even though oxidation of the highly reactive sharp edges could not be completely avoided. However, the combination of UV/vis/NIR and theoretical modeling give strong evidence that the observed overgrowth can be clearly divided into completely separated processes: (I) growth and (II) edge sharpening.

Quantitative Analysis of the Overgrowth Kinetics. In the following, we investigated the influence of the surfactant headgroup on the kinetics of overgrowth. Thus, we employed a master curve to evaluate the time-dependent volume change from the experimental UV/vis/NIR data (see Figure S9). Figure 5 shows the evolution of the particle volume over time for both surfactants. The volume change shows a sigmoidal behavior as expected for surface-controlled growth reac-

DOI: 10.1021/acs.jpcc.5b03155
J. Phys. Chem. C 2015, 119, 9513–9523

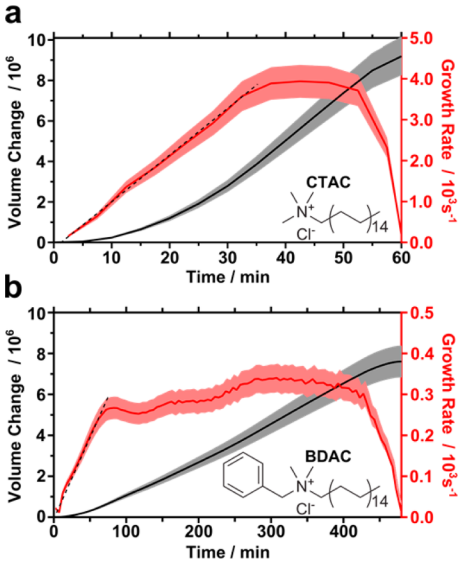

Figure 5. Surfactant-controlled overgrowth kinetics in (a) CTAC and (b) BDAC: volume change $\Delta V/V_{Ag^0}$ (black), i.e., the number of reduced ions N_{Ag^0}, over time. The corresponding growth rates (red), given by the first derivative dN_{Ag0}/dt, exhibit three growth regimes: increasing growth rate, constant growth rate, and the cease of growth. Please note changes in scaling.

tions.[61,62] The volume change over time is given by the number of silver ions (N_{Ag^+}) reduced to elementary silver (N_{Ag^0}) at the particle surface times the volume of a single silver atom V_{Ag^0} (0.0125 nm^3).[82]

$$\frac{dV}{dt} = V_{Ag^0}\frac{dN_{Ag^0}}{dt} \quad \text{with} \quad \frac{dN_{Ag^0}}{dt} = -\frac{dN_{Ag^+}}{dt} \tag{1}$$

At first glance, it becomes apparent that the overgrowth proceeds in CTAC faster than in BDAC by a factor of 8. The respective maximum growth rates differ by about a single order of magnitude. Generally, the overgrowth proceeds similar for both surfactants: First, the growth rate increases linearly with time. The acceleration of the growth rate in BDAC (0.05 ± 0.01 nm^3/s^2) is about 30 times slower than in CTAC (1.4 ± 0.1 nm^3/s^2). Subsequently, the volume increases at nearly constant growth rates (CTAC, 48 ± 5 nm^3/s; BDAC, 4 ± 1 nm^3/s).[61] Finally, the growth rate decreases successively until the final volume is obtained. From the theoretical modeling, we can infer that late stages of the overgrowth process are dominated by shape changes of the particles, i.e., edge sharpening. Consequently, the master curve is only valid within the actual growth regime (see Figure S9). At this point, we can formulate a generalized silver overgrowth mechanism in the context of surfactant-controlled kinetics.

Figure 6 gives a schematic representation of the generalized silver overgrowth mechanism, which involves three main processes: (1) the micellar diffusion of surfactant-stabilized Ag^+ ions (Ag^+@micelle) in bulk solution, (2) the transport of ions across the fluid surfactant bilayer, and (3) the reduction of ions at the metal surface. In regard to the first process, both surfactants form micelles of different aggregation numbers (BDAC 62, CTAC 101)[58] but of comparable sizes (radius 3 nm, SAXS) in water.[59] Thus, similar diffusion rates can be expected in bulk solution above the critical micellar concentration. The resulting diffusion coefficient of 7.6 × 10^{-11} m^2/s for such a micelle would result in much faster

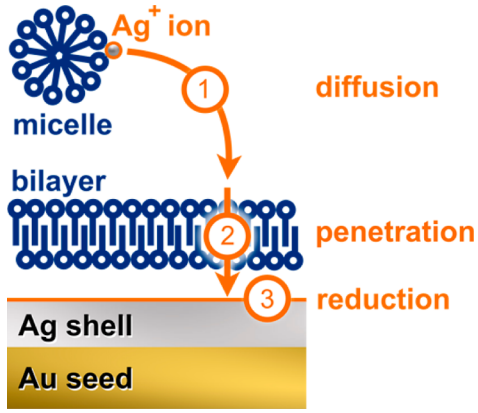

Figure 6. Schematic representation of the three-step silver overgrowth mechanism.

reaction kinetics for a purely diffusion-limited regime.[61] Thus, micellar diffusion (step 1) is not rate-limiting as it can be expected to allow for a steady supply of ions from solution indifferent of the surfactant. Therefore, the significant difference in reaction kinetics observed for BDAC and CTAC can be attributed to either the bilayer transition (surfactant−surfactant interactions; step 2) or the reduction at the surface (ion-surfactant interactions; step 3), or a balance of both.

In regard to step 2, the fluid surfactant bilayer at the particle surface acts as a stabilizing membrane. Hence, differences in membrane stiffness could significantly affect ion supply. The effective membrane stiffness not only arises from the molecular packing density and thermodynamics but also gains from distinct headgroup interactions. For BDAC, these are $\pi-\pi$ interactions of the benzyl substituents. However, a lower packing density (due to bulky headgroups) may be balanced by intermolecular interactions. In regard to step 3, Ag^+ exhibits higher binding affinity toward BDAC owing to cation−π interactions of the electron-rich benzyl headgroup.[83] The aromatic complexation might inhibit the reduction of Ag^+@BDAC compared to Ag^+@CTAC.

To solve the question whether the bilayer transition (step 2) or the reduction at the surface (step 3), or a balance of both, is rate determining requires further in-depth studies. Nevertheless, the presented approach can be used as a generic concept to determine growth rates of nanoparticle synthesis *in situ* even for complex morphologies. In addition, our results have great potential for tailoring of reaction rates by a rational choice of surfactants.

Plasmonic Modes of Au@Ag Cuboids. With an experimental control of the overgrowth process it is possible to fabricate tailored plasmonic Au@Ag cuboid modes. Figure 7a shows resonance frequencies of all dominant plasmonic modes during the overgrowth process and the corresponding changes in aspect ratio. Furthermore, we compared the plasmonic modes from the overgrowth process with a pure silver cuboid to emphasize the influence of the gold core. Figure 7b shows the surface charge distributions relative to their excited wavelength. The gold nanorod exhibits two dipolar modes, which are defined as zeroth-order modes (subscript 0) with respect to their exciting polarization (superscript L/T). The identical mode signatures are present for the pure silver cuboid of zeroth order. Because of sharper edges in comparison to the nanorod, we observe two further, higher dipolar modes (subscript 1−2). These so-called cubic plasmonic modes are

DOI: 10.1021/acs.jpcc.5b03155
J. Phys. Chem. C 2015, 119, 9513−9523

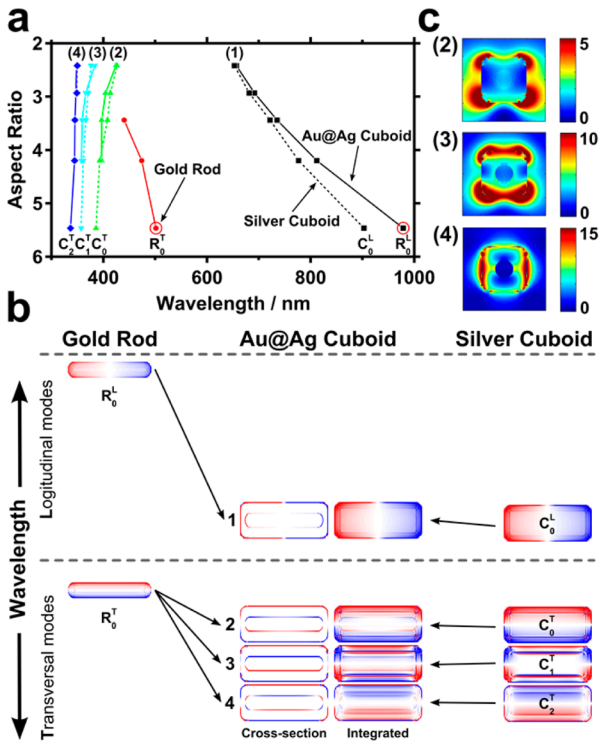

Figure 7. (a) Plasmonic modes evaluated from simulated extinction spectra for increasing aspect ratios for gold nanorod overgrowth with silver (solid lines) and pure silver cuboid (intersected lines). (b) Plasmonic modes (surface charge distribution) of the gold nanorod, Au@Ag cuboid, and pure silver cuboid relative to their excitation wavelength. (c) Electric field distribution of transversal modes of the Au@Ag cuboid. The edge rounding was fixed to 8%.

well-known and described in more detail elsewhere.[80,84] As expected from the overgrowth process, the silver cuboid modes are dominating the gold nanorod mode, which results in a significant blue-shift of the gold nanorod mode. However, the resulting Au@Ag cuboid modes are different to the cuboid modes without gold core in respect to their excited polarization and wavelength. The longitudinal Au@Ag cuboid mode exhibits the same charge distribution at the gold nanorod core and the silver cuboid shell (in-phase charges). In contrast, all transversal Au@Ag cuboid modes exhibit opposite charges at the core in respect to the shell (mirror charges).

These induced mirror charges at the gold nanorod core in respect to the silver cuboid shell are correlated with the complex permittivity ($\varepsilon = \varepsilon' + i\varepsilon''$) of the used materials (see Figure S10). The induced mirror charges of the transversal Au@Ag cuboid modes occur between the band overlap of the intraband of silver (326 nm) and the interband of gold (515 nm). At this wavelength range the damping of gold is significantly higher compared to silver (ε''), whereas the polarizability follows the same trend (ε'). It is important to note that in the interband region of gold the real part of permittivity is at the limit for surface plasmon resonances (nonradiative condition) as described by Raether.[85] Briefly, for a non-radiative condition the real part of the metal must be negative and smaller as the permittivity of the environment ($\varepsilon' < -\varepsilon_{medium}$), in our case water ($\varepsilon_{H_2O} = 1.77$). In the interband of gold the permittivity falls below the non-radiative condition with increasing energy (see Figure S10). Consequently, the induced mirror charges are getting stronger at lower wavelength (Figure 7b,c). More details of the transversal modes could be found in the Supporting Information (Figures S11−13 and Text S1). This significant difference in damping and polarizability at the overlap region renders the gold core a retarded plasmonic element compared to the silver shell. If this finding is transferred to an antenna-receiver model, the silver shell can be described as antenna, which transmits its electromagnetic field to the gold core (receiver). To the best of our knowledge, this antenna effect at the metal/metal interface of core/shell particles has not been reported in the literature so far.

Following the plasmonic mode (2) during the overgrowth process reveals that the induced mirror charges already occur at a very thin silver layer (see Figure 8). These two modes at 474 nm (in-phase charged) and 397 nm (mirror charged) are also

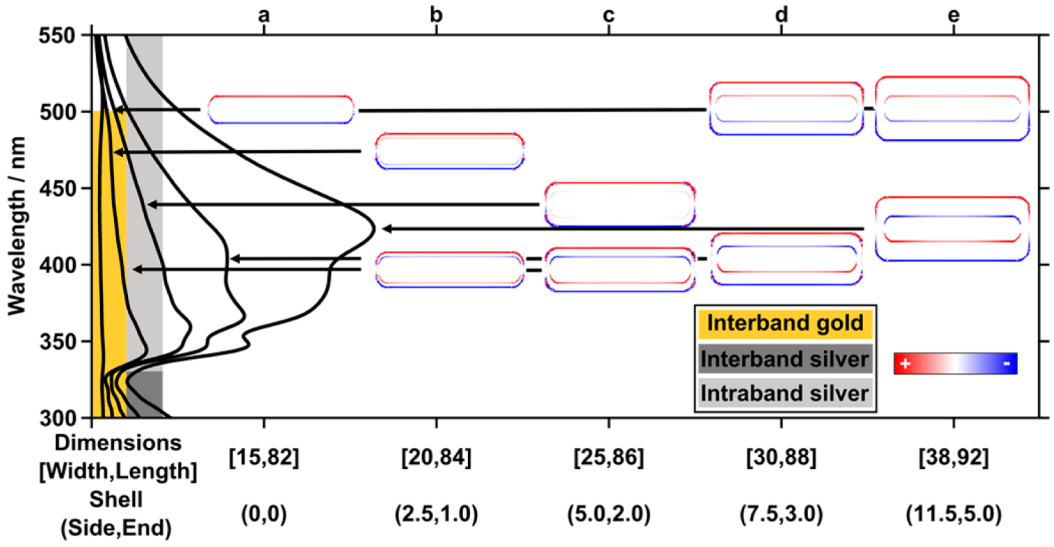

Figure 8. Evolution of plasmonic mode (2) during the tailored overgrowth process to emphasize the nature of in-phase and mirror charges. The mirror charges occur exclusively in the overlap region of interband and intraband of gold and silver, respectively. Surface charge distribution plots of (a) the gold nanorod core and (b−e) Au@Ag cuboids of different dimensions [width/length] and shell thicknesses (side/end). All units are in nanometers.

DOI: 10.1021/acs.jpcc.5b03155
J. Phys. Chem. C 2015, 119, 9513−9523

recognizable as peaks in the extinction cross section. With a further shell overgrowth only the mirror charged mode is visible in the extinction cross section (Figure 8c–e). To excite the in-phase charge distribution (Figure 8e), the core must be excited at its resonance wavelength (502 nm) with a small bandwidth 33 THz (28 nm). The antenna effect has the same signature as the bonding and antibonding mode described by the hybridization model from Prodan et al.[20] Comparing the Au@Ag cuboid mirror charges with a hybridization model observed for stacked double crescents reveals two advantages:[2] All modes are in the optical visible spectrum, and the energetic difference between the modes is about a factor of 3 smaller. Consequently, with full control during the overgrowth the silver shell could be fine-tuned to the wavelength of interest. These building blocks with intrinsic metamaterial properties have potential for application in metamaterials, if self-assembled to clusters (trimer and heptamer assemblies) or modified by facet-selective etching to break the symmetry and form split-ring-resonator-like structures. This paves the road for new strategies to develop cost-efficient syntheses of nanophotonic structures, which exhibit strong mirror-charge responses or Fano-like resonances, similar to metal/dielectric cluster assemblies.[86]

CONCLUSION

The close correlation of transient morphological and optical changes during overgrowth of gold nanorods with a cuboidal silver shell is a straightforward approach to thoroughly explain *in situ* kinetics recorded with UV/vis/NIR spectroscopy. This approach enabled us to compare two different surfactants namely CTAC and BDAC with respect to their impact on nanoparticle growth behavior. Static experiments revealed almost no differences in nanoparticle quality for both surfactants since the overall growth mechanism and the final shape is dictated by the counterion chloride in combination with the Au to Ag ratio. Selective stabilization of {100} facets lead to nanoparticle overgrowth into Au@Ag cuboids as reported elsewhere.[45,71] However, the surfactants show significant differences in their overgrowth kinetics. The overgrowth rate of BDAC is about an order of magnitude lower compared to CTAC. This can be directly related to the headgroup structure as aromatics strongly influence the kinetics of nanoparticle syntheses. Detailed investigation revealed that the overgrowth kinetics can be divided in three stages: (I) accelerated growth, (II) constant growth rate, and (III) deceleration going along with edge sharpening. Furthermore, we found that edge rounding is a good indicator for quality of the performed synthesis. These results will help to further increase understanding of nanoparticle syntheses and overgrowth processes. In addition, this knowledge offers the possibility to fine-tune and enhance control for nanoparticle synthesis and overgrowth reactions. Investigation of the plasmonic modes revealed that the presence of the gold nanorod core inside the silver cuboid alters the resulting resonances. These Au@Ag cuboid modes feature in-phase and mirror-charged plasmonic modes. The latter might be of particular interest for metamaterial design due to their induced mirror charge nature, which is a prerequisite for negative permeability.

ASSOCIATED CONTENT

Supporting Information

TEM characterization of gold nanorods and Au@Ag cuboids; 3D plots of the UV/vis/NIR data of the dynamic growth experiments; FDTD modeling of gold nanorods and Au@Ag cuboids, and their dynamic growth kinetics; systematic evaluation of the UV/vis/NIR data of the dynamic experiments based on the results of the static experiments; complex permittivity of Ag and Au; further information about mirror charges at the gold/silver interface of core/shell particles; electric field intensity cross sections and plane-plots; silver overgrowth synthesis parameters. This material is available free of charge via the Internet at http://pubs.acs.org.

AUTHOR INFORMATION

Corresponding Authors

*(T.K.) E-mail: tobias.koenig@uni-bayreuth.de.
*(A.F.) E-mail: andreas.fery@uni-bayreuth.de.

Notes

The authors declare no competing financial interest.

ACKNOWLEDGMENTS

This work was funded by the European Research Council under grant ERC-2012-StG 306686 (METAMECH: Template-assisted assembly of METAmaterials using MECHanical instabilities) and PRIOSERS FP7MC-IEF-623527, and by the German Science Foundation within the SFB 840. M.T. was supported by the Elite Network Bavaria in the frame of the Elite Study Program “Macromolecular Science” and funded via a grant for Ph.D. candidates according to Bavarian elite promotion law (BayEFG). The authors thank C. Kunert for performing TEM measurements.

REFERENCES

(1) Liu, N.; Hentschel, M.; Weiss, T.; Alivisatos, A. P.; Giessen, H. Three-Dimensional Plasmon Rulers. *Science* **2011**, *332*, 1407–1410.
(2) Liu, N.; Weiss, T.; Mesch, M.; Langguth, L.; Eigenthaler, U.; Hirscher, M.; Sönnichsen, C.; Giessen, H. Planar Metamaterial Analogue of Electromagnetically Induced Transparency for Plasmonic Sensing. *Nano Lett.* **2009**, *10*, 1103–1107.
(3) Hao, F.; Nordlander, P.; Sonnefraud, Y.; Dorpe, P. V.; Maier, S. A. Tunability of Subradiant Dipolar and Fano-Type Plasmon Resonances in Metallic Ring/Disk Cavities: Implications for Nanoscale Optical Sensing. *ACS Nano* **2009**, *3*, 643–652.
(4) Anker, J. N.; Hall, W. P.; Lyandres, O.; Shah, N. C.; Zhao, J.; Van Duyne, R. P. Biosensing with Plasmonic Nanosensors. *Nat. Mater.* **2008**, *7*, 442–453.
(5) Oulton, R. F.; Sorger, V. J.; Zentgraf, T.; Ma, R.-M.; Gladden, C.; Dai, L.; Bartal, G.; Zhang, X. Plasmon Lasers at Deep Subwavelength Scale. *Nature* **2009**, *461*, 629–632.
(6) Pacifici, D.; Lezec, H. J.; Atwater, H. A. All-Optical Modulation by Plasmonic Excitation of Cdse Quantum Dots. *Nat. Photonics* **2007**, *1*, 402–406.
(7) Linic, S.; Christopher, P.; Ingram, D. B. Plasmonic-Metal Nanostructures for Efficient Conversion of Solar to Chemical Energy. *Nat. Mater.* **2011**, *10*, 911–921.
(8) Karg, M.; König, T. A. F.; Retsch, M.; Stelling, C.; Reichstein, P. M.; Honold, T.; Thelakkat, M.; Fery, A. Colloidal Self-Assembly Concepts for Light Management in Photovoltaics. *Mater. Today* **2014**, DOI: 10.1016/j.mattod.2014.10.036.
(9) Cai, W.; Shalaev, V. *Optical Metamaterials - Fundamentals and Applications*; Springer: Berlin, 2010; p 200.
(10) Rockstuhl, C.; Lederer, F.; Etrich, C.; Zentgraf, T.; Kuhl, J.; Giessen, H. On the Reinterpretation of Resonances in Split-Ring-Resonators at Normal Incidence. *Opt. Express* **2006**, *14*, 8827–8836.

DOI: 10.1021/acs.jpcc.5b03155
J. Phys. Chem. C 2015, 119, 9513–9523

(11) Shelby, R. A.; Smith, D. R.; Schultz, S. Experimental Verification of a Negative Index of Refraction. *Science* **2001**, *292*, 77−79.
(12) Soukoulis, C. M.; Wegener, M. Past Achievements and Future Challenges in the Development of Three-Dimensional Photonic Metamaterials. *Nat. Photonics* **2011**, *5*, 523−530.
(13) Hanske, C.; Tebbe, M.; Kuttner, C.; Bieber, V.; Tsukruk, V. V.; Chanana, M.; König, T. A. F.; Fery, A. Strongly Coupled Plasmonic Modes on Macroscopic Areas Via Template-Assisted Colloidal Self-Assembly. *Nano Lett.* **2014**, *14*, 6863−6871.
(14) Kraus, T.; Brodoceanu, D.; Pazos-Perez, N.; Fery, A. Colloidal Surface Assemblies: Nanotechnology Meets Bioinspiration. *Adv. Funct. Mater.* **2013**, *23*, 4529−4541.
(15) Nordlander, P. The Ring: A Leitmotif in Plasmonics. *ACS Nano* **2009**, *3*, 488−492.
(16) Wang, H.; O'Dea, K.; Wang, L. Selective Absorption of Visible Light in Film-Coupled Nanoparticles by Exciting Magnetic Resonance. *Opt. Lett.* **2014**, *39*, 1457−1460.
(17) Dolling, G.; Enkrich, C.; Wegener, M.; Zhou, J. F.; Soukoulis, C. M.; Linden, S. Cut-Wire Pairs and Plate Pairs as Magnetic Atoms for Optical Metamaterials. *Opt. Lett.* **2005**, *30*, 3198−3200.
(18) Kuznetsov, A. I.; Miroshnichenko, A. E.; Fu, Y. H.; Zhang, J.; Luk'yanchuk, B. Magnetic Light. *Sci. Rep.* **2012**, *2*, 492.
(19) Wang, H.; Brandl, D. W.; Le, F.; Nordlander, P.; Halas, N. J. Nanorice: A Hybrid Plasmonic Nanostructure. *Nano Lett.* **2006**, *6*, 827−832.
(20) Prodan, E.; Radloff, C.; Halas, N. J.; Nordlander, P. A Hybridization Model for the Plasmon Response of Complex Nanostructures. *Science* **2003**, *302*, 419−422.
(21) Chen, H.; Shao, L.; Li, Q.; Wang, J. Gold Nanorods and Their Plasmonic Properties. *Chem. Soc. Rev.* **2013**, *42*, 2679−2724.
(22) Gómez-Graña, S.; Goris, B.; Altantzis, T.; Fernańdez-Lopez, C.; Carbo-Argibay, E.; Guerrero-Martínez, A.; Almora-Barrios, N.; Lopez, N.; Pastoriza-Santos, I.; Perez-Juste, J.; et al. Au@Ag Nanoparticles: Halides Stabilize {100} Facets. *J. Phys. Chem. Lett.* **2013**, *4*, 2209−2216.
(23) Hou, S.; Hu, X.; Wen, T.; Liu, W.; Wu, X. Core−Shell Noble Metal Nanostructures Templated by Gold Nanorods. *Adv. Mater.* **2013**, *25*, 3857−3862.
(24) Lohse, S. E.; Burrows, N. D.; Scarabelli, L.; Liz-Marzán, L. M.; Murphy, C. J. Anisotropic Noble Metal Nanocrystal Growth: The Role of Halides. *Chem. Mater.* **2013**, *26*, 34−43.
(25) Hao, J.; Qingfeng, Z.; Nicolas, L.; Chunmei, Y.; Douglas, A. B.; Peter, N.; Hui, W. Tunable Plasmonic Nanoparticles with Catalytically Active High-Index Facets. *Nano Lett.* **2014**, *14*, 3674−3682.
(26) Park, K.; Drummy, L. F.; Vaia, R. A. Ag Shell Morphology on Au Nanorod Core: Role of Ag Precursor Complex. *J. Mater. Chem.* **2011**, *21*, 15608.
(27) Xia, Y.; Xiong, Y.; Lim, B.; Skrabalak, S. E. Shape-Controlled Synthesis of Metal Nanocrystals: Simple Chemistry Meets Complex Physics? *Angew. Chem., Int. Ed.* **2009**, *48*, 60−103.
(28) Nikoobakht, B.; El-Sayed, M. A. Preparation and Growth Mechanism of Gold Nanorods (NRs) Using Seed-Mediated Growth Method. *Chem. Mater.* **2003**, *15*, 1957−1962.
(29) Jana, N. R.; Gearheart, L.; Murphy, C. J. Seed-Mediated Growth Approach for Shape-Controlled Synthesis of Spheroidal and Rod-Like Gold Nanoparticles Using a Surfactant Template. *Adv. Mater.* **2001**, *13*, 1389−1393.
(30) Vigderman, L.; Zubarev, E. R. High-Yield Synthesis of Gold Nanorods with Longitudinal Spr Peak Greater Than 1200 Nm Using Hydroquinone as a Reducing Agent. *Chem. Mater.* **2013**, *25*, 1450−1457.
(31) Vigderman, L.; P. Khanal, B.; R. Zubarev, E. Functional Gold Nanorods: Synthesis, Self-Assembly, and Sensing Applications. *Adv. Mater.* **2012**, *24*, 4811−4841.
(32) Grzelczak, M.; Perez-Juste, J.; Mulvaney, P.; Liz-Marzan, L. M. Shape Control in Gold Nanoparticle Synthesis. *Chem. Soc. Rev.* **2008**, *37*, 1783−1791.
(33) Müller, M. B.; Kuttner, C.; König, T. A. F.; Tsukruk, V. V.; Förster, S.; Karg, M.; Fery, A. Plasmonic Library Based on Substrate-Supported Gradiential Plasmonic Arrays. *ACS Nano* **2014**, *8*, 9410−9421.
(34) Ye, X.; Jin, L.; Caglayan, H.; Chen, J.; Xing, G.; Zheng, C.; Doan-Nguyen, V.; Kang, Y.; Engheta, N.; Kagan, C. R.; et al. Improved Size-Tunable Synthesis of Monodisperse Gold Nanorods through the Use of Aromatic Additives. *ACS Nano* **2012**, *6*, 2804−2817.
(35) Scarabelli, L.; Grzelczak, M.; Liz-Marzán, L.; Tuning Gold, M. Nanorod Synthesis through Prereduction with Salicylic Acid. *Chem. Mater.* **2013**, *25*, 42324238.
(36) Khlebtsov, B. N.; Khanadeev, V. A.; Ye, J.; Sukhorukov, G. B.; Khlebtsov, N. G. Overgrowth of Gold Nanorods by Using a Binary Surfactant Mixture. *Langmuir* **2014**, *30*, 1696−1703.
(37) Ye, X.; Zheng, C.; Chen, J.; Gao, Y.; Murray, C. B. Using Binary Surfactant Mixtures to Simultaneously Improve the Dimensional Tunability and Monodispersity in the Seeded Growth of Gold Nanorods. *Nano Lett.* **2013**, *13*, 765−771.
(38) DuChene, J. S.; Niu, W.; Abendroth, J. M.; Sun, Q.; Zhao, W.; Huo, F.; Wei, W. D. Halide Anions as Shape-Directing Agents for Obtaining High-Quality Anisotropic Gold Nanostructures. *Chem. Mater.* **2012**, *25*, 1392−1399.
(39) Grzelczak, M.; Sánchez-Iglesias, A.; Rodríguez-González, B.; Alvarez-Puebla, R.; Pérez-Juste, J.; Liz-Marzán, L. M. Influence of Iodide Ions on the Growth of Gold Nanorods: Tuning Tip Curvature and Surface Plasmon Resonance. *Adv. Funct. Mater.* **2008**, *18*, 3780−3786.
(40) Millstone, J. E.; Wei, W.; Jones, M. R.; Yoo, H.; Mirkin, C. A. Iodide Ions Control Seed-Mediated Growth of Anisotropic Gold Nanoparticles. *Nano Lett.* **2008**, *8*, 2526−2529.
(41) Almora-Barrios, N.; Novell-Leruth, G.; Whiting, P.; Liz-Marzán, L. M.; López, N. Theoretical Description of the Role of Halides, Silver, and Surfactants on the Structure of Gold Nanorods. *Nano Lett.* **2014**, *14*, 871−875.
(42) Si, S.; Leduc, C.; Delville, M.-H.; Lounis, B. Short Gold Nanorod Growth Revisited: The Critical Role of the Bromide Counterion. *ChemPhysChem* **2012**, *13*, 193−202.
(43) Xu, D.; Jianfeng, Z.; Xiaoyun, L.; Danli, L.; Liusheng, Z. Preparation of Monodisperse Bimetallic Nanorods with Gold Nanorod Core and Silver Shell and Their Plasmonic Property and Sers Efficiency. *J. Raman Spectrosc.* **2014**, *45*, 431−437.
(44) Gómez-Graña, S.; Pérez-Juste, J.; Alvarez-Puebla, R. A.; Guerrero-Martínez, A.; Liz-Marzán, L. M. Self-Assembly of Au@Ag Nanorods Mediated by Gemini Surfactants for Highly Efficient Sers-Active Supercrystals. *Adv. Opt. Mater.* **2013**, *1*, 477−481.
(45) Jiang, R.; Chen, H.; Shao, L.; Li, Q.; Wang, J. Unraveling the Evolution and Nature of the Plasmons in (Au Core)-(Ag Shell) Nanorods. *Adv. Mater.* **2012**, *24*, 200−207.
(46) Gong, J.; Zhou, F.; Li, Z.; Tang, Z. Synthesis of Au@Ag Core−Shell Nanocubes Containing Varying Shaped Cores and Their Localized Surface Plasmon Resonances. *Langmuir* **2012**, *28*, 8959−8964.
(47) Yoshifumi, O.; Koji, N.; Ayaka, K.; Naotoshi, N.; Ayumu, I.; Yasuro, N. Uniform and Controllable Preparation of Au−Ag Core−Shell Nanorods Using Anisotropic Silver Shell Formation on Gold Nanorods. *Nanoscale* **2010**, *2*, 1489−1493.
(48) Goris, B.; De Backer, A.; Van Aert, S.; Gómez-Graña, S.; Liz-Marzán, L. M.; Van Tendeloo, G.; Bals, S. Three-Dimensional Elemental Mapping at the Atomic Scale in Bimetallic Nanocrystals. *Nano Lett.* **2013**, *13*, 4236−4241.
(49) Carbó-Argibay, E.; Rodríguez-González, B.; Gómez-Graña, S.; Guerrero-Martínez, A.; Pastoriza-Santos, I.; Pérez-Juste, J.; Liz-Marzán, L. M. The Crystalline Structure of Gold Nanorods Revisited: Evidence for Higher-Index Lateral Facets. *Angew. Chem., Int. Ed.* **2010**, *49*, 9397−9400.
(50) Kou, X.; Zhang, S.; Tsung, C.-K.; Yang, Z.; Yeung, M. H.; Stucky, G. D.; Sun, L.; Wang, J.; Yan, C. One-Step Synthesis of Large-Aspect-Ratio Single-Crystalline Gold Nanorods by Using CTPAB and CTAB Surfactants. *Chem.—Eur. J.* **2007**, *13*, 2929−2936.

DOI: 10.1021/acs.jpcc.5b03155
J. Phys. Chem. C 2015, 119, 9513−9523

(51) Gómez-Graña, S.; Hubert, F.; Testard, F.; Guerrero-Martínez, A.; Grillo, I.; Liz-Marzán, L. M.; Spalla, O. Surfactant (Bi)Layers on Gold Nanorods. *Langmuir* **2011**, *28*, 1453−1459.
(52) Nikoobakht, B.; El-Sayed, M. A. Evidence for Bilayer Assembly of Cationic Surfactants on the Surface of Gold Nanorods. *Langmuir* **2001**, *17*, 6368−6374.
(53) Murphy, C. J.; Thompson, L. B.; Alkilany, A. M.; Sisco, P. N.; Boulos, S. P.; Sivapalan, S. T.; Yang, J. A.; Chernak, D. J.; Huang, J. The Many Faces of Gold Nanorods. *J. Phys. Chem. Lett.* **2010**, *1*, 2867−2875.
(54) Lohse, S. E.; Murphy, C. J. The Quest for Shape Control: A History of Gold Nanorod Synthesis. *Chem. Mater.* **2013**, *25*, 1250−1261.
(55) Zhang, L.; Xia, K.; Lu, Z.; Li, G.; Chen, J.; Deng, Y.; Li, S.; Zhou, F.; He, N. Efficient and Facile Synthesis of Gold Nanorods with Finely Tunable Plasmonic Peaks from Visible to Near-IR Range. *Chem. Mater.* **2014**, *26*, 1794−1798.
(56) Sinnokrot, M. O.; Sherrill, C. D. High-Accuracy Quantum Mechanical Studies of Π−Π Interactions in Benzene Dimers. *J. Phys. Chem. A* **2006**, *110*, 10656−10668.
(57) Sinnokrot, M. O.; Sherrill, C. D. Unexpected Substituent Effects in Face-to-Face Π-Stacking Interactions. *J. Phys. Chem. A* **2003**, *107*, 8377−8379.
(58) Alargova, R. G.; Kochijashky, I. I.; Zana, R. Fluorescence Study of the Aggregation Behavior of Different Surfactants in Aqueous Solutions in the Presence and in the Absence of Gas. *Langmuir* **1998**, *14*, 1575−1579.
(59) Park, K.; Koerner, H.; Vaia, R. A. Depletion-Induced Shape and Size Selection of Gold Nanoparticles. *Nano Lett.* **2010**, *10*, 1433−1439.
(60) Pérez-Juste, J.; Liz-Marzán, L. M.; Carnie, S.; Chan, D. Y. C.; Mulvaney, P. Electric-Field-Directed Growth of Gold Nanorods in Aqueous Surfactant Solutions. *Adv. Funct. Mater.* **2004**, *14*, 571−579.
(61) Henkel, A.; Schubert, O.; Plech, A.; Sonnichsen, C. Growth Kinetic of a Rod-Shaped Metal Nanocrystal. *J. Phys. Chem. C* **2009**, *113*, 10390−10394.
(62) Zijlstra, P.; Bullen, C.; Chon, J. W. M.; Gu, M. High-Temperature Seedless Synthesis of Gold Nanorods. *J. Phys. Chem. B* **2006**, *110*, 19315−19318.
(63) Gulati, A.; Liao, H.; Hafner, J. H. Monitoring Gold Nanorod Synthesis by Localized Surface Plasmon Resonance. *J. Phys. Chem. B* **2006**, *110*, 22323−22327.
(64) Novo, C.; Funston, A. M.; Mulvaney, P. Direct Observation of Chemical Reactions on Single Gold Nanocrystals Using Surface Plasmon Spectroscopy. *Nat. Nanotechnol.* **2008**, *3*, 598−602.
(65) Becker, J.; Zins, I.; Jakab, A.; Khalavka, Y.; Schubert, O.; Sönnichsen, C. Plasmonic Focusing Reduces Ensemble Linewidth of Silver-Coated Gold Nanorods. *Nano Lett.* **2008**, *8*, 1719−1723.
(66) Becker, J.; Schubert, O.; Sönnichsen, C. Gold Nanoparticle Growth Monitored in Situ Using a Novel Fast Optical Single-Particle Spectroscopy Method. *Nano Lett.* **2007**, *7*, 1664−1669.
(67) Sau, T. K.; Murphy, C. J. Seeded High Yield Synthesis of Short Au Nanorods in Aqueous Solution. *Langmuir* **2004**, *20*, 6414−6420.
(68) Herrmann, L. O.; Baumberg, J. J. Watching Single Nanoparticles Grow in Real Time through Supercontinuum Spectroscopy. *Small* **2013**, *9*, 3743−3747.
(69) Morita, T.; Tanaka, E.; Inagaki, Y.; Hotta, H.; Shingai, R.; Hatakeyama, Y.; Nishikawa, K.; Murai, H.; Nakano, H.; Hino, K. Aspect-Ratio Dependence on Formation Process of Gold Nanorods Studied by Time-Resolved Distance Distribution Functions. *J. Phys. Chem. C* **2010**, *114*, 3804−3810.
(70) Edgar, J. A.; McDonagh, A. M.; Cortie, M. B. Formation of Gold Nanorods by a Stochastic "Popcorn" Mechanism. *ACS Nano* **2012**, *6*, 1116−1125.
(71) Hubert, F.; Testard, F.; Thill, A.; Kong, Q.; Tache, O.; Spalla, O. Growth and Overgrowth of Concentrated Gold Nanorods: Time Resolved SAXS and XANES. *Cryst. Growth Des.* **2012**, *12*, 1548−1555.
(72) Okuno, Y.; Nishioka, K.; Kiya, A.; Nakashima, N.; Ishibashi, A.; Niidome, Y. Uniform and Controllable Preparation of Au-Ag Core-Shell Nanorods Using Anisotropic Silver Shell Formation on Gold Nanorods. *Nanoscale* **2010**, *2*, 1489−1493.
(73) Johnson, P. B.; Christy, R. W. Optical Constants of the Noble Metals. *Phys. Rev. B* **1972**, *6*, 4370−4379.
(74) Hagemann, H. J.; Gudat, W.; Kunz, C. Optical Constants from the Far Infrared to the X-Ray Region: Mg, Al, Cu, Ag, Au, Bi, C, and $A1_2O_3$. *J. Opt. Soc. Am. A* **1975**, *65*, 742−744.
(75) Goris, B.; Bals, S.; Van den Broek, W.; Carbó-Argibay, E.; Gómez-Graña, S.; Liz-Marzán, L. M.; Van Tendeloo, G. Atomic-Scale Determination of Surface Facets in Gold Nanorods. *Nat. Mater.* **2012**, *11*, 930−935.
(76) Huang, C.-C.; Yang, Z.; Chang, H.-T. Synthesis of Dumbbell-Shaped Au−Ag Core−Shell Nanorods by Seed-Mediated Growth under Alkaline Conditions. *Langmuir* **2004**, *20*, 6089−6092.
(77) Mushran, S. P.; Agrawal, M. C.; Mehrotra, R. M.; Sanehi, R. Kinetics and Mechanism of Reduction of Silver(I) by Ascorbic Acid. *J. Chem. Soc.* **1974**, 1460−1462.
(78) Gupta, M. K.; König, T.; Near, R.; Nepal, D.; Drummy, L. F.; Biswas, S.; Naik, S.; Vaia, R. A.; El-Sayed, M. A.; Tsukruk, V. V. Surface Assembly and Plasmonic Properties in Strongly Coupled Segmented Gold Nanorods. *Small* **2013**, *9*, 2979−2990.
(79) Im, S. H.; Lee, Y. T.; Wiley, B.; Xia, Y. Large-Scale Synthesis of Silver Nanocubes: The Role of HCl in Promoting Cube Perfection and Monodispersity. *Angew. Chem., Int. Ed.* **2005**, *44*, 2154−2157.
(80) Kodiyath, R.; Malak, S. T.; Combs, Z. A.; Koenig, T.; Mahmoud, M. A.; El-Sayed, M. A.; Tsukruk, V. V. Assemblies of Silver Nanocubes for Highly Sensitive Sers Chemical Vapor Detection. *J. Mater. Chem. A* **2013**, *1*, 2777−2788.
(81) König, T.; Kodiyath, R.; Combs, Z. A.; Mahmoud, M. A.; El-Sayed, M. A.; Tsukruk, V. V. Silver Nanocube Aggregates in Cylindrical Pores for Higher Refractive Index Plasmonic Sensing. *Part. Part. Syst. Charact.* **2014**, *31*, 274−283.
(82) Aylward, G. H.; Findlay, T. J. V. *Datensammlung Chemie in Si Einheiten*; Wiley-VCH: Weinheim, 1999; Vol. 3.
(83) Ma, J. C.; Dougherty, D. A. The Cation−Π Interaction. *Chem. Rev.* **1997**, *97*, 1303−1324.
(84) Zhang, S.; Bao, K.; Halas, N. J.; Xu, H.; Nordlander, P. Substrate-Induced Fano Resonances of a Plasmonic: Nanocube: A Route to Increased-Sensitivity Localized Surface Plasmon Resonance Sensors Revealed. *Nano Lett.* **2011**, *11*, 1657−1663.
(85) Raether, H. *Surface Plasmons on Smooth and Rough Surfaces and on Gratings*; Springer: Berlin, 1988.
(86) Fan, J. A.; Wu, C.; Bao, K.; Bao, J.; Bardhan, R.; Halas, N. J.; Manoharan, V. N.; Nordlander, P.; Shvets, G.; Capasso, F. Self-Assembled Plasmonic Nanoparticle Clusters. *Science* **2010**, *328*, 1135−1138.

DOI: 10.1021/acs.jpcc.5b03155
J. Phys. Chem. C 2015, 119, 9513−9523